Hybrid Acoustic Topological Insulator in Three Dimensions

Cheng He,[1,3,§] Si-Yuan Yu,[1,3,§] Huaiqiang Wang,[2,§] Hao Ge,[1] Jiawei Ruan,[2] Haijun Zhang,[2,3,*] Ming-Hui Lu,[1,3,4,†] and Yan-Feng Chen[1,3,‡]

[1]*National Laboratory of Solid State Microstructures & Department of Materials Science and Engineering, Nanjing University, Nanjing 210093, China*

[2]*National Laboratory of Solid State Microstructures & School of Physics, Nanjing University, Nanjing 210093, China*

[3]*Collaborative Innovation Center of Advanced Microstructures, Nanjing University, Nanjing 210093, China*

[4]*Jiangsu Key Laboratory of Artificial Functional Materials, Nanjing University, Nanjing 210093, China*

(Received 23 April 2019; published 6 November 2019)

Topological insulators (TIs), featured by a symmetry-protected gapless surface Dirac cone(s) in their complete energy band gaps, have been extended from condensed-matter physics to classical bosonic systems in the last decade. However, acoustic TIs in three dimensions remain elusive because of a lack of a spin or polarization degree of freedom for longitudinal airborne sound. Here, we experimentally demonstrate a feasible way to hybridize an acoustic TI in three dimensions based on band inversion through a three-dimensional (3D) hybrid Dirac point (HDP). Such a 3D HDP, with linear dispersion in the layer plane while quadratic out of the layer, is distinct from a general point with linear dispersion in all directions. Interestingly, a single nearly gapless conical-like dispersion for acoustic surface states can be achieved at both zigzag and armchair interfaces, supporting robust sound transport. Our findings can serve as a tabletop platform for exploring unique acoustic applications based on the two-dimensional topological interfaces.

DOI: 10.1103/PhysRevLett.123.195503

The topological design for the band structures of solid-state materials has drawn great interest [1,2], and has been extended to various classical wave systems in the last decade, including photonics [3–9], mechanics [10–15], and acoustics [16–22]. One well-known case is the topological insulator (TI), which can exhibit spin-momentum locking; i.e., different spins transport in opposite directions, protected by time-reversal symmetry. To date, various kinds of classical wave TIs have been successfully explored in two-dimensional (2D) systems, benefiting from artificial symmetries. Their one-dimensional (1D) gapless edge states have shown broad application prospects, such as robust optical or acoustic waveguides [23–26], topologically directional antennas [27,28], and arbitrary shaped topological lasers [29,30]. Naturally, the quest for three-dimensional (3D) classical wave TIs is open, which can provide us 2D topological planes to manipulate waves.

Despite many efforts to realize 3D photonic TIs [31–34], a 3D acoustic TI is still a challenge. The difficulty is coming from the spinless nature of airborne sound, which poses a serious limit to directly mimic 3D TI as those in photonic systems via magneto-optical materials [32] or electromagnetic coupling [33,34]. Although the acoustic pseudospins can be artificially generated by using multiple acoustic sources with different phase delays [35,36], to make it topological may refer to certain symmetry of structures. Previous studies have shown that 2D acoustic topological states with acoustic pseudospins can be realized relying on the construction of some special spatial symmetry [26,37]. However, it is difficult to directly stack them to form 3D acoustic TIs because the interlayer coupling will destroy the spatial symmetry based pseudospins [38]. On the other hand, although the Weyl [39,40] and the third order topological states [41,42] have shown the intriguing physics in 3D acoustic systems, their ungapped bulk states or gapped corner states cannot be used to simultaneously confine and guide sound. Therefore, a 3D acoustic TI, which provides 2D gapless topological surface states in a full bulk band gap, is increasingly desirable.

In this Letter, we report our acoustic TI in a 3D acoustic crystal consisting of double-layer honeycomb lattices. By characterizing the intra- and interlayer coupling, a full acoustic bulk band gap is created associated with band inversion. In the band gap, we observe a single nearly gapless conical-like surface dispersion on the lateral interface to support robust sound transport. Our unique surface states possess discretionally linear fashion, i.e., linear in the plane while nonlinear out of the plane, the so-called 3D hybrid acoustic TI. Our work extends the scope of acoustic TI from two to three dimensions, paving a way to engineer the dispersion of 2D topological surface states. Such hybrid topological surface states with nonlinear dispersion as well as the strongly backscattering suppressed behavior can be used to realize directional slow sound and high-efficiency acoustic delay lines.

Different from a Dirac [43] or Weyl [39,44] system with linear dispersion along all directions, here we consider a

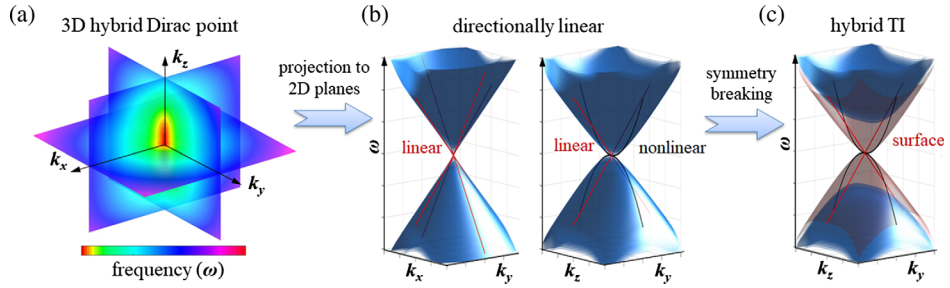

FIG. 1. (a) Schematic of a 3D hybrid Dirac point for bulk bands, where the color scale represents frequency. (b) Projection hybrid Dirac cone to the k_{xy} and k_{zy} planes, where the red or black line shows linear or nonlinear dispersion along different directions. (C) Hybrid TI case after symmetry breaking, where the red surface represents the directionally linear surface states.

kind of hybrid case in three dimensions [Fig. 1(a)] whose bulk band dispersion is linear along the k_x/k_y but nonlinear along the k_z direction as shown in Fig. 1(b), also known as semi-Dirac cones [45–47]. After opening a topological bulk band gap, we can obtain a hybrid TI in three dimensions as shown in Fig. 1(c). Although the surface dispersion is directionally linear, the surface state can be gapless to support robust wave transport.

Our acoustic crystal is constructed by a double-layer honeycomb lattice, as shown in Fig. 2(a). The A layer (denoted in blue) consists of identical atoms, while the B layer (denoted in green) consists of alternating two atoms. The hexagonal unit cell contains 12 atoms (9 blue and 3 red atoms) with the lattice constant a. The side length of the inner dashed hexagon is b. Figure 2(b) shows one-half of the first bulk Brillouin zone (BZ) and its surface BZ when projected onto an armchair (100) surface or zigzag (010) surface. The triangular prism cavities with different side lengths represent two acoustic atoms shown in Fig. 2(c). The intralayer and interlayer couplings of neighboring atoms are represented by connecting tubes. The hexagonal unit cell in Fig. 2(a) with 12 acoustic atoms is 3 times larger than a primary unit cell with 4 acoustic atoms [48]. Such a larger unit cell used here is to increase the pseudospin degree of freedom for spinless sound. Thus, we can create fourfold degenerate Bloch states that guarantee a pair of acoustic pseudospins based on the sublattice symmetry [9].

By stretching and compressing the inner hexagons in the xy plane without changing the size of the unit cell [9], we can manipulate the hopping effect between neighboring unit cells to realize bulk band inversion, as shown in Fig. 2(d). In the trivial insulator case in which $b/a = 0.57$ (compressing), *d-type* acoustic states are located in the upper two bands, and *p-type* acoustic states are located in the lower two bands [Fig. 2(e)], separated by a complete bulk band gap. Here, the *d-type* acoustic states obey the same symmetries relative to the x and y axes (both even or both odd), while the *p-type* acoustic states obey the opposite symmetries relative to the x and y axes (either even or odd). The side lengths l_b and l_r are chosen to be $0.69a$ and $0.92a$, respectively, with other parameters established as follows: height $h = 1.54a$, prism height $h_p = 0.31a$, and tube diameter $r = 0.27a$. At the topological transition point $b/a = 2/3$, as shown in Fig. 2(f), a fourfold degenerate point is formed at the A point based on the BZ folding mechanism [48]. The bulk bands are inverted when $b/a = 0.73$ (stretching), as shown in Fig. 2(g); i.e., the *d-type* acoustic states are located in the lower two bands, and the *p-type* bands are located in the upper two bands, indicating the existence of topological surface states in the nontrivial complete bulk band gap. It should be noted that such a fourfold degenerate point is a type of hybrid Dirac point, which shows linear dispersions in the k_{xy} plane but quadratic dispersion along the k_z axis in the vicinity of the A point [46].

To study the acoustic topological surface states, we introduce a zigzag interface, as illustrated in Fig. 2(h) between topologically trivial [Fig. 2(e)] and nontrivial [Fig. 2(g)] acoustic crystals. The blue region in Fig. 2(i) represents the overlapping pass bulk bands of two acoustic crystals with a complete band gap frequency ranging from 0.38 to $0.41(2\pi c/a)$. Notably, there exists a pair of acoustic surface states nearly touching at the $\tilde{Z}$ point [red lines in Fig. 2(i)] over the entire surface BZ. A magnified 3D view of acoustic surface states near the $\tilde{Z}$ point [Fig. 2(j)] clearly shows conical-like dispersion.

Although a tiny surface band gap, with a relative bandwidth of less than 0.2%, appears in the surface state, this surface state still possesses strongly backscattering suppressed sound transport inherited from the topology of the bulk bands. From a physical point of view, the topology of our 3D acoustic model is originated from the rotation symmetry of in-plane honeycomb layer (C_6 symmetry of the A layer) [9,48], which cannot be satisfied on a lateral 2D surface. Therefore, the surface dispersion is by no means gapless under arbitrary surface configuration [49]. However, in a special case, there may exist a mirror symmetry normal to the surface, which can make the surface states gapless (with nontrivial mirror winding numbers) [50,51]. Our theoretical tight-binding lattice model verifies that no obvious surface band gap can be found [48]. On the other hand, the finite size of acoustic atoms and the finite periods of acoustic crystals also contribute to the surface band gap. And, it can be further decreased by tuning the geometry parameters [26].

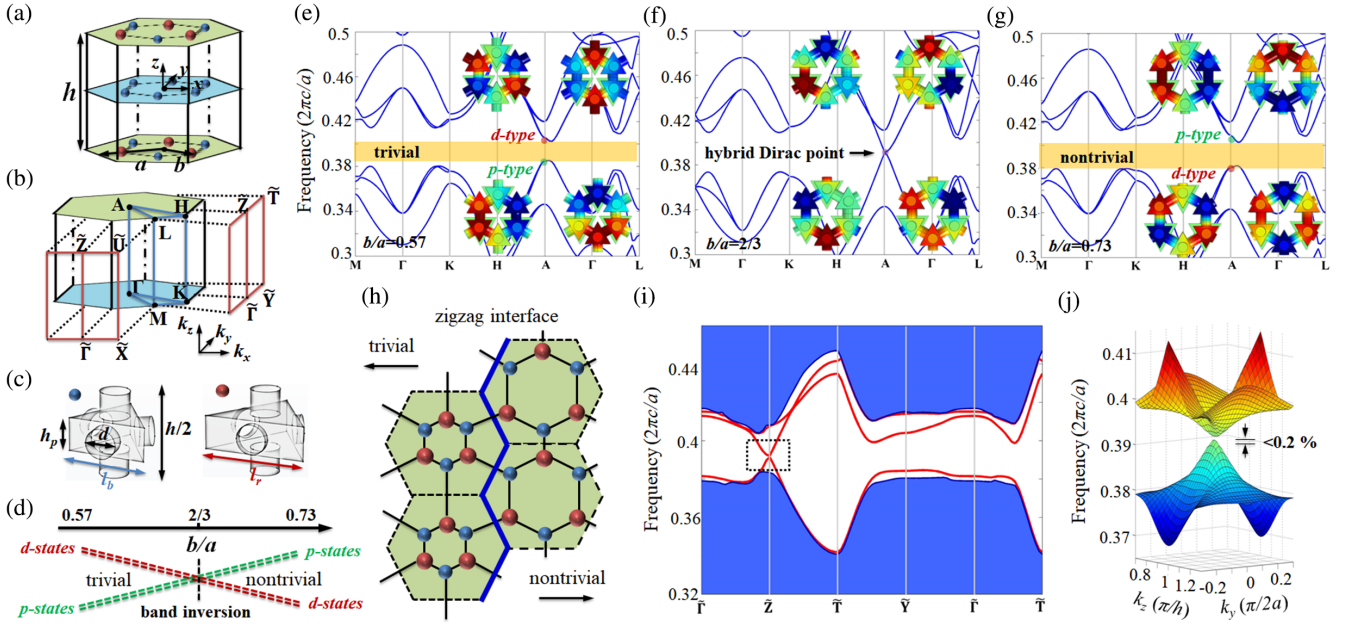

FIG. 2. (a) Schematic of the atomic structure of acoustic crystal constructed by double-layer honeycomb lattice. The A layer (blue) is formed by identical atoms, and the B layer (green) is formed by two different atoms. (b) One-half of the bulk BZ and surface BZ in the k_{yz} plane (100-surface BZ) and k_{xz} plane (010-surface BZ). (c) The triangular prism cavities and connecting tubes represent the acoustic atoms and their couplings. (d) Bands inversion by stretching and compressing in the xy plane. (e)–(g), Bulk band structures at (e), $b/a = 0.57$, (f), $b/a = 2/3$, and (g), $b/a = 0.73$. Insets show top-down views of the acoustic states of the A layer. (h) Schematic of the zigzag interface with topological trivial and nontrivial acoustic crystals. (i) The projected band structures, where the blue regions represent the overlapping bulk pass band and the red lines represent the topological surface states. (j) 3D view of acoustic surface states near the $\tilde{Z}$ point with a tiny surface band gap of less than 0.2%.

Figure 3(a) shows our experimental sample with lattice constant $a = 1$ cm, where the topologically trivial acoustic crystal residing on the left part and the nontrivial one residing on the right form a zigzag interface supporting robust acoustic transport (illustrated by a blue line). Each acoustic crystal has 11.5×10 unit cells in the xy plane and 8 unit cells along the z direction with full dimensions of $17.25 \times 17.32 \times 12.32$ cm. Figure 3(b) is our experimental configuration to measure directional transmission spectra of surface states. Here, three 2D k slices on the conical-like surface Dirac cone with different angles are chosen to check the robust acoustic propagations, as shown in Fig. 3(c). In experiments, we measured the bulk transmission spectra for the trivial and nontrivial acoustic crystals with the bulk band gap frequency region from 12.5 to 14.4 kHz (ΓA direction), as indicated by the black and gray lines in Fig. 3(d). Regarding acoustic surface transmission, it can be observed that for slice 1 [the red line in Fig. 3(d)], our data show that the transmission consistently remains high over the entire bulk band gap frequency region, indicating nearly gapless behavior (the tiny surface band gap cannot be detected due to the finite size). For slices 2 and 3, two transmission dips exist near a frequency of 13.5 kHz [the cyan and blue lines in Fig. 3(d)], showing directional gapped surface states. The frequencies for the upper and lower edges of the surface transmission dips correspond to the bottom of the upper branch and the top of the lower one for the surface states, respectively [dots in Fig. 3(c)]. Notably, from slice 3 to slice 1, the surface transmission dips are gradually reduced, confirming the nearly gapless behavior of acoustic surface states along the k_y direction.

To further confirm the surface dispersion along the k_z direction ($k_y = 0$), we experimentally measured the surface acoustic field distributions along the z direction (20 periods) at the open boundary of the 2D topological interface (air-crystals interface) [52] at various frequencies as shown in Fig. 3(e). The corresponding Bloch momentum can be obtained by the Fourier transformation of the field distribution at a specific frequency to form the surface band dispersion along the $\tilde{\Gamma}\tilde{Z}$ direction [red line in Fig. 3(f)]. Thus, we can clearly observe a pair of surface dispersions merging at the $\tilde{Z}$ point ($k_z = \pi/h$), as shown in Fig. 3(g). A small influence originates from the scattered acoustic wave into the air. We also measure the dispersion for air from 12.8 to 15.2 kHz to confirm that the Brillouin boundary $k_z = \pi/h$ is not crossed [48]. It is worth noting that only in the vicinity of the $\tilde{Z}$ point is the surface dispersion along the k_z direction quadratic; away from this point, the dispersion is mainly linear.

The acoustic topological surface states of our 3D acoustic crystals can exist not only in the zigzag but also

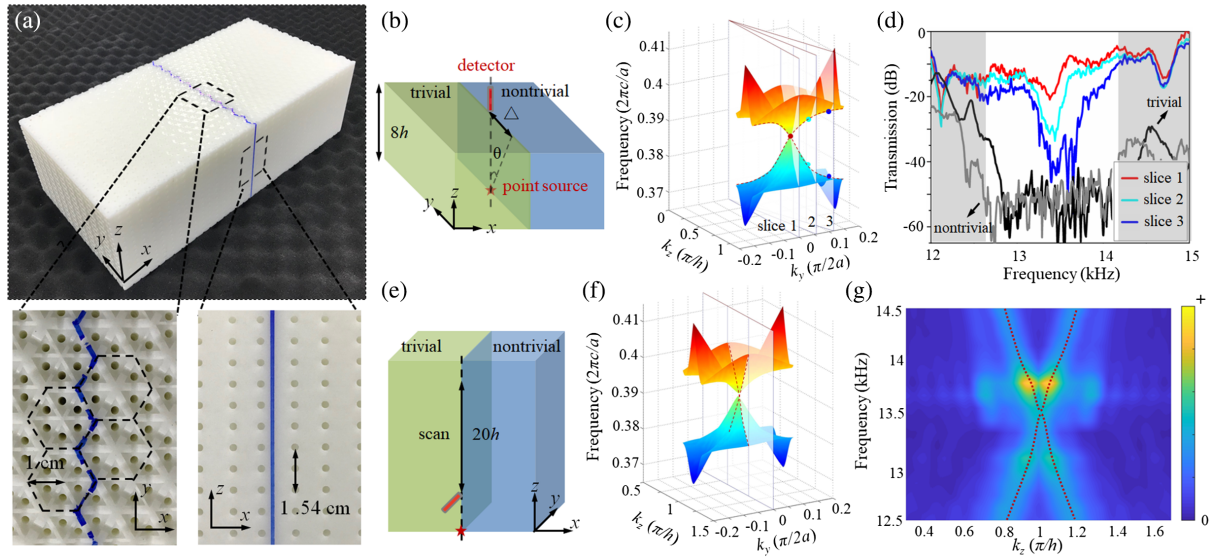

FIG. 3. (a) Images of the experimental sample. Lower left: magnified top-down view. Lower right: magnified lateral view. Blue lines indicate the interface. (b) Experimental configuration to measure directional transmission spectra of surface states, where θ represents the angle. (c) Three 2D-k slices on conical-like surface dispersion with $\theta = 0$, $\arctan(0.5a/8h)$ and $\arctan(a/8h)$, corresponding to $\Delta = 0$, 0.5, and 1 cm in the experiments, respectively. (d) Experimentally measured transmission spectra. The black and gray lines correspond to the bulk band transmission of two acoustic crystals along the ΓA direction, where the shadow regions indicate the overlap of the bulk pass band. The surface transmission spectra for slices 1–3 are represented by red, cyan, and blue lines, respectively. (e) Experimental configuration to map the surface dispersion along the $\tilde{\Gamma}\,\tilde{Z}$ direction. (f) A slice at $k_y = 0$. (g) The measured surface dispersion. The color scale represents the energy density. The dashed lines are drawn to guide the eye.

armchair interfaces. Figure 4(a) shows a schematic of the armchair interface between topologically trivial and nontrivial acoustic crystals. We can still find a pair of acoustic surface states nearly touching at the $\tilde{Z}$ point [red lines in Fig. 4(b)]. Figure 4(c) shows the 3D view of conical-like surface dispersion near the $\tilde{Z}$ point. The measured acoustic surface dispersion along the $\tilde{\Gamma}\,\tilde{Z}$ direction is shown in Fig. 4(d), which agrees well with our simulated results.

In summary, we have demonstrated 3D topological acoustic crystals with conical-like acoustic surface states in the complete bulk band gap. At the $k_z = \pi/h$ plane, each layer is decoupled; i.e., thus the A layer with uniform atoms will exhibit an acoustic quantum pseudospin Hall effect along the k_x and k_y boundaries, which resembles the 2D TI case. Meanwhile, due to the existence of a mirror plane along the z axis, the acoustic pseudospin associated with surface pseudospin locking can be constructed along the k_z direction as well [36]. Therefore, our directional topological model can be treated as a type of hybrid acoustic TI in three dimensions, which can support robust sound transport with little backscattering in the arbitrary 2D lateral interface.

Compared to the nonreciprocal 2D acoustic quantum Hall effect (with nontrivial first Chern numbers) by using circular air flow to break time-reversal symmetry [16,17,53], our passive 3D acoustic model is time-reversal invariant, where the acoustic pseudospin locking is originated from

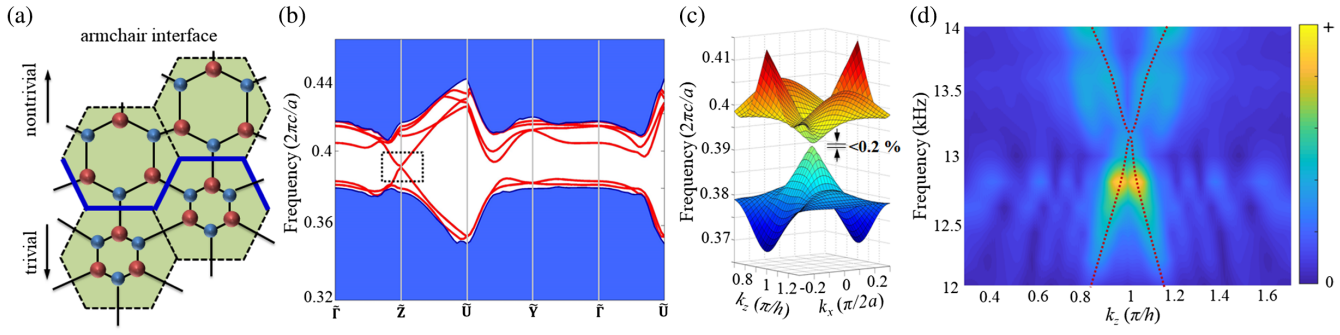

FIG. 4. (a) Schematic of armchair interface. (b) The projected band structures, where the red lines represent the surface states. (c) 3D view of surface states near the $\tilde{Z}$ point. (d) The measured surface dispersion at the slice of $k_x = 0$. The color scale represents the energy density. The dashed lines are drawn to guide the eye.

the spatial symmetry construction. By considering nonreciprocity and additional synthetic dimensions in 3D acoustic models, it is also feasible to realize the high-dimensional topological phenomena in the acoustic systems, such as the four-dimensional quantum Hall effect with nontrivial second Chern numbers [54–56].

In contrast to the recently realized 3D photonic weak TIs with even numbers of surface Dirac cones [34], our 3D acoustic model only possesses a single conical-like surface dispersion. Although a rigorous 3D TI for bosonic system (in the term of a single surface Dirac cone) may require broken time-reversal symmetry with magnets or exotic bi-anisotropic materials [8], our passive acoustic topological model based solely on spatial symmetry can bypass many of the materials limitations and implementation hurdles. Our work opens a door to study acoustic TI in 3D structures, where 230 types of space groups can be involved. Furthermore, no need to resort to an intrinsic spin or polarization degree of freedom, such a concept can be readily extended to any other spinless system. The ability of manipulating hybrid surface dispersion we demonstrated here provides the opportunity to explore novel topological behaviors and unique applications, such as directionally slow sound, robust acoustic surface sensing and imaging based on the 2D topological interfaces [49].

The work was jointly supported by the National Key R&D Program of China (Grant No. 2017YFA0305100 and 2017YFA0303702) and the National Natural Science Foundation of China (Grant No. 11874196, 11890700, 11674165, 11625418, 51732006, 51721001, and 51702152). We also acknowledge the support of the Fundamental Research Funds for the Central Universities (Grant No. 021314380097, 021314380143, and 020414380038) and the Fok Ying-Tong Education Foundation of China (Grant No. 161006).

*Corresponding author.
zhanghj@nju.edu.cn
†Corresponding author.
luminghui@nju.edu.cn
‡Corresponding author.
yfchen@nju.edu.cn
§C. H., S.-Y. Y., H. W. contributed equally to this work.

[1] M. Z. Hasan and C. L. Kane, Rev. Mod. Phys. **82**, 3045 (2010).
[2] X.-L. Qi and S.-C. Zhang, Rev. Mod. Phys. **83**, 1057 (2011).
[3] F. D. M. Haldane and S. Raghu, Phys. Rev. Lett. **100**, 013904 (2008).
[4] Z. Wang, Y. Chong, J. D. Joannopoulos, and M. Soljačić, Nature (London) **461**, 772 (2009).
[5] L. Lu, J. D. Joannopoulos, and M. Soljacic, Nat. Photonics **8**, 821 (2014).
[6] M. C. Rechtsman, J. M. Zeuner, Y. Plotnik, Y. Lumer, D. Podolsky, F. Dreisow, S. Nolte, M. Segev, and A. Szameit, Nature (London) **496**, 196 (2013).
[7] M. Hafezi, S. Mittal, J. Fan, A. Migdall, and J. M. Taylor, Nat. Photonics **7**, 1001 (2013).
[8] T. Ozawa *et al.*, Rev. Mod. Phys. **91**, 015006 (2019).
[9] L.-H. Wu and X. Hu, Phys. Rev. Lett. **114**, 223901 (2015).
[10] C. L. Kane and T. C. Lubensky, Nat. Phys. **10**, 39 (2014).
[11] R. Süsstrunk and S. D. Huber, Science **349**, 47 (2015).
[12] S. D. Huber, Nat. Phys. **12**, 621 (2016).
[13] R. K. Pal and M. Ruzzene, New J. Phys. **19**, 025001 (2017).
[14] T.-W. Liu and F. Semperlotti, Phys. Rev. Applied **9**, 014001 (2018).
[15] R. Chaunsali, C.-W. Chen, and J. Yang, New J. Phys. **20**, 113036 (2018).
[16] Z. Yang, F. Gao, X. Shi, X. Lin, Z. Gao, Y. Chong, and B. Zhang, Phys. Rev. Lett. **114**, 114301 (2015).
[17] A. B. Khanikaev, R. Fleury, S. H. Mousavi, and A. Alù, Nat. Commun. **6**, 8260 (2015).
[18] M. Xiao, W.-J. Chen, W.-Y. He, and C. T. Chan, Nat. Phys. **11**, 920 (2015).
[19] Y.-G. Peng, C.-Z. Qin, D.-G. Zhao, Y.-X. Shen, X.-Y. Xu, M. Bao, H. Jia, and X.-F. Zhu, Nat. Commun. **7**, 13368 (2016).
[20] M. Serra-Garcia, V. Peri, R. Süsstrunk, O. R. Bilal, T. Larsen, L. G. Villanueva, and S. D. Huber, Nature (London) **555**, 342 (2018).
[21] J. Lu, C. Qiu, L. Ye, X. Fan, M. Ke, F. Zhang, and Z. Liu, Nat. Phys. **13**, 369 (2017).
[22] Z. Zhang, Y. Cheng, and X. Liu, Sci. Rep. **8**, 16784 (2018).
[23] A. B. Khanikaev, S. H. Mousavi, W.-K. Tse, M. Kargarian, A. H. MacDonald, and G. Shvets, Nat. Mater. **12**, 233 (2013).
[24] W.-J. Chen, S.-J. Jiang, X.-D. Chen, B. Zhu, L. Zhou, J.-W. Dong, and C. T. Chan, Nat. Commun. **5**, 5782 (2014).
[25] X. Cheng, C. Jouvaud, X. Ni, S. H. Mousavi, A. Z. Genack, and A. B. Khanikaev, Nat. Mater. **15**, 542 (2016).
[26] C. He, X. Ni, H. Ge, X.-C. Sun, Y.-B. Chen, M.-H. Lu, X.-P. Liu, and Y.-F. Chen, Nat. Phys. **12**, 1124 (2016).
[27] Z. Zhang, Y. Tian, Y. Wang, S. Gao, Y. Cheng, X. Liu, and J. Christensen, Adv. Mater. **30**, 1803229 (2018).
[28] F. Gao, H. Xue, Z. Yang, K. Lai, Y. Yu, X. Lin, Y. Chong, G. Shvets, and B. Zhang, Nat. Phys. **14**, 140 (2018).
[29] M. A. Bandres, S. Wittek, G. Harari, M. Parto, J. Ren, M. Segev, D. N. Christodoulides, and M. Khajavikhan, Science **359**, eaar4005 (2018).
[30] B. Bahari, A. Ndao, F. Vallini, A. El Amili, Y. Fainman, and B. Kanté, Science **358**, 636 (2017).
[31] Q. Lin, X.-Q. Sun, M. Xiao, S.-C. Zhang, and S. Fan, Sci. Adv. **4**, eaat2774 (2018).
[32] L. Lu, C. Fang, L. Fu, S. G. Johnson, J. D. Joannopoulos, and M. Soljačić, Nat. Phys. **12**, 337 (2016).
[33] A. Slobozhanyuk, S. H. Mousavi, X. Ni, D. Smirnova, Y. S. Kivshar, and A. B. Khanikaev, Nat. Photonics **11**, 130 (2017).
[34] Y. Yang, Z. Gao, H. Xue, L. Zhang, M. He, Z. Yang, R. Singh, Y. Chong, B. Zhang, and H. Chen, Nature (London) **565**, 622 (2019).
[35] F. H. Busse and T. G. Wang, J. Acoust. Soc. Am. **69**, 1634 (1981).
[36] C. Shi, R. Zhao, Y. Long, S. Yang, Y. Wang, H. Chen, J. Ren, and X. Zhang, Nat. Sci. Rev. **6**, 707 (2019).

[37] J. Lu, C. Qiu, W. Deng, X. Huang, F. Li, F. Zhang, S. Chen, and Z. Liu, Phys. Rev. Lett. **120**, 116802 (2018).
[38] C. He *et al.*, Nat. Commun. **9**, 4555 (2018).
[39] F. Li, X. Huang, J. Lu, J. Ma, and Z. Liu, Nat. Phys. **14**, 30 (2018).
[40] H. He, C. Qiu, L. Ye, X. Cai, X. Fan, M. Ke, F. Zhang, and Z. Liu, Nature (London) **560**, 61 (2018).
[41] H. Xue, Y. Yang, G. Liu, F. Gao, Y. Chong, and B. Zhang, Phys. Rev. Lett. **122**, 244301 (2019).
[42] M. Weiner X. Ni, M. Li, A. Alù, and A. B. Khanikaev, arXiv:1903.00428.
[43] Q. Guo, B. Yang, L. Xia, W. Gao, H. Liu, J. Chen, Y. Xiang, and S. Zhang, Phys. Rev. Lett. **119**, 213901 (2017).
[44] B. Yang *et al.*, Science **359**, 1013 (2018).
[45] Y. Wu, Opt. Express **22**, 1906 (2014).
[46] V. Pardo and W. E. Pickett, Phys. Rev. Lett. **102**, 166803 (2009).
[47] H. Huang, Z. Liu, H. Zhang, W. Duan, and D. Vanderbilt, Phys. Rev. B **92**, 161115 (2015).
[48] See Supplemental Material at http://link.aps.org/supplemental/10.1103/PhysRevLett.123.195503 for information on theoretical model, additional simulated results, measurements, and methods.
[49] L. Lu, J. D. Joannopoulos, and M. Soljačić, Nat. Phys. **12**, 626 (2016).
[50] T. Kariyado and X. Hu, Sci. Rep. **7**, 16515 (2017).
[51] T. Kariyado and R.-J. Slager, arXiv:1903.08638v1 [Phys. Rev. Lett. (to be published)].
[52] S. Yves, R. Fleury, F. Lemoult, M. Fink, and G. Lerosey, New J. Phys. **19**, 075003 (2017).
[53] Y. Ding, Y. Peng, Y. Zhu, X. Fan, J. Yang, B. Liang, and X. Zhu, X. Wan, and J. Cheng, Phys. Rev. Lett. **122**, 014302 (2019).
[54] L. Lu, H. Gao, and Z. Wang, Nat. Commun. **9**, 5384 (2018).
[55] O. Zilberberg, S. Huang, J. Guglielmon, M. Wang, K. P. Chen, Y. E. Kraus, and M. C. Rechtsman, Nature (London) **553**, 59 (2018).
[56] X. Fan, C. Qiu, Y. Shen, H. He, M. Xiao, M. Ke, and Z. Liu, Phys. Rev. Lett. **122**, 136802 (2019).